Int J Adv Manuf Technol (2002) 19:587–596

The International Journal of
Advanced
Manufacturing
Technology

Influence of Punch Radius and Angle on the Outward Curling Process of Tubes

You-Min Huang and Yuung-Ming Huang

Department of Mechanical Engineering, National Taiwan University of Science and Technology, Taipei, Taiwan

Using the theory of updated Lagrangian formulation, this study adopted the elasto-plastic finite-element method and extended the increment determination method, the r_{min} *method, to include the element's yielding, nodal contact with or separation from the tool, maximum strain and limit of rotation increment. The computer code for a finite-element method is established using the modified Coulomb's friction law. Conical punches with different radii and angles are used in the forming simulation of hard copper and brass tube ends. The effects of various elements including the half-apex angle of punch (*α*) and its radius (*R*), the ratio of the thickness of the tube wall to the mean diameter of tube, mechanical properties, and lubrication on the tube's outward curling, are investigated. Simulation findings indicate that when the bending radius at the punch inlet (*ρ*) satisfies the condition of* $\rho \leqq \rho_c$*, curling is present at the tube end. On the other hand, if* $\rho \geqq \rho_c$*, the tube end experiences flaring. The variable* ρ_c *is called the critical bending radius. The value of* ρ_c *increases as the value of* α *increases. Furthermore, the findings also show that* ρ_c *is neither correlated with tube material nor lubrication.*

Keywords: Elasto-plastic; Finite elements; Half-apex angle; Outward-curling process

1. Introduction

The process of forming convex edges of a metal tube is often employed for connecting two tube parts, linking and locking a tube part and its components, and connecting fluid pipelines or combining complementary pipelines with reinforcement at the tube's end. It is a common industrial technology related to tube ends. The tube end processes are generally divided into tapper flaring, flange flaring, step flaring, and curl forming. The tube-curling deformation discussed in this paper curls the opening of the tube's end outward in a circle. The simulation of the tube-curling deformation is a complex and difficult task because the deformation process is highly nonlinear. The nonlinear deformation characteristic is due to:

1. The large displacement, rotation, and deformation during metal deformation.
2. The nonlinear material deformation behaviour when metal material experiences large deformation.
3. The nonlinear boundary condition generated by the friction between the metal and tool interface, and their contact conditions.

These characteristics made the finite-element method the most widely used of the metal process analyses. To improve the process and increase industrial productivity, this study developed an elasto-plastic finite-element computer code using the selective reduced integration (SRI) simulation method, which employs four integral point elements within the four nodes of a rectangle. The objective is to simulate the tube-curling deformation process.

Nadai [1] studied tube-nosing in 1943. The theoretical induction was an extension of the curved shell theory. Nadai assumed the friction coefficient to be constant, and ignored the presence of effective stress variation in the shell. Cruden and Tompson [2] conducted a series of tube-nosing experiments to establish the various limitations of tube-nosing and evaluate the effects of various parameters. Manabe and Nishimura [3–7] also conducted a series of experiments on both conical tube-flaring and tube-nosing processes to investigate the effects of various parameters on the forming load and stress–strain distribution. The parameters studied include the conical punch with different angles, lubrication, material and tube wall thickness. Tang and Kobayashi [8] proposed a rigid-plastic finite-element theory and developed a computer code to simulate the cold-nosing of 105 mm AISI 1018 steel. Huang et al. [9] simulated the cold-nosing process through elasto-plastic and rigid-plastic finite-element methods and compared the simulation results with experimental data to verify the accuracy of the rigid-plastic finite element. Kitazawa et al. [10,11] conducted experiments with conical punches, and copper and brass materials with the assumption that the tube materials were rigid-perfectly plastic. They had explored previously the effect of the arc radius of

Correspondence and offprint requests to: Dr You-Min Huang, Department of Mechanical Engineering, National Taiwan University of Science and Technology, Taipei, Taiwan. E-mail: ymhuang@mail.ntust.edu.tw

the punch, angle, and tube wall thickness on the tube-curling deformation process. Kitazawa [12] used carbon steel, copper, and brass as the tube materials in his experiment of tube-curling deformation. When the flaring energy increment at the front edge of the tube end (δW_f) is greater than the energy increment at the curl edge (δW_c), the tube end material undergoes outward curling forming because of the absence of unbending. On the other hand, if $\delta W_c \geqq \delta W_f$, the tube end material is attached to the conical punch surface because of unbending and fails to curl or form flaring. The energy rule was used to induce the deformation energy at the time of tube forming for the purpose of comparison and verification, thus establishing the criterion of outward curling.

In this study, the same material constants and dimensions used in other studies [12] are adopted in the simulation of the outward curling process. The findings are compared with the results reported in [12] to verify the accuracy of the elasto-plastic finite-element computer code developed.

2. Description of the Basic Theory

2.1 Stiffness Equation

Adopting the updated Lagrangian formulation (ULF) in the framework of the application of incremental deformation for the metal forming process (bulk forming and sheet forming) is the most practical approach for describing the incremental characteristics of the plastic flow rule. The current configuration in ULF at each deformation stage is used as the reference state for evaluating the deformation for a small time interval Δt such that first-order theory is consistent with the accuracy requirement.

The virtual work rate equation of the updated Lagrangian equation is written as

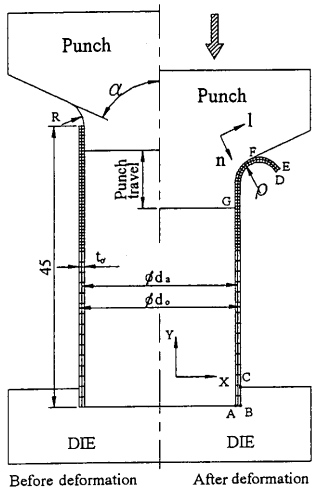

Fig. 1. Boundary conditions for the deformation tubes geometry of outward curling at an initial and a particular stage. Units, mm; R, punch radius; α, half-apex punch angle; ρ, bending radius at punch inlet.

$$\int_V (\tau_{ij}^* - 2\sigma_{ik}\dot{\epsilon}_{kj})\,\delta\dot{\epsilon}_{ij}\mathrm{d}V + \int_V \sigma_{jk}L_{ik}\delta L_{ij}\mathrm{d}V = \int_{S_f} \dot{\bar{t}}_i \delta v_i \mathrm{d}S \tag{1}$$

where τ_{ij}^* is the Jaumann rate of Kirchhoff stress, σ_{ij} is the Cauchy stress, $\dot{\epsilon}_{ij}$ is the rate of deformation which is the Cartesian coordinate, v_i is the velocity, $\dot{\bar{t}}_i$ is the rate of the nominal traction, L_{ij} $(= \partial v_i/\partial X_j)$ is the velocity gradient, X_j is the spatial fixed Cartesian coordinate, V and S_f are the material volume and the surface on which the traction is prescribed.

The J_2 flow rule

$$\tau^* = \frac{E}{1+v}\left[\delta_{ik}\delta_{jl} + \frac{v}{1-2v}\,\delta_{ij}\delta_{kl} - \frac{3\lambda(E/(1+v))\,\sigma'_{ij}\sigma'_{kl}}{2\bar{\sigma}^2\,(\frac{2}{3}H' + E/(1+v))}\right]\dot{\epsilon}_{kl} \tag{2}$$

is employed to model the elasto-plastic behaviour of sheet metal, where H' is the strain hardening rate, $\bar{\sigma}$ is the effective stress, E is the Young's modulus, v is the Poisson's ratio, σ'_{ij} is the deviatoric part of σ_{ij}. λ takes 1 for the plastic state and 0 for the elastic state or the unloading.

It is assumed that the distribution of the velocity $\{v\}$ in a discretised element is

$$\{v\} = [N]\,\{\dot{d}\} \tag{3}$$

where $[N]$ is the shape function matrix and $\{\dot{d}\}$ denotes the nodal velocity. The rate of deformation and the velocity gradient are written as

$$\{\dot{\epsilon}\} = [B]\,\{\dot{d}\} \tag{4}$$

$$\{L\} = \{E\}\,\{\dot{d}\} \tag{5}$$

where $[B]$ and $[E]$ represent the strain rate–velocity matrix and the velocity gradient–velocity matrix, respectively. Substituting Eqs (4) and (5) into Eq. (1), the elemental stiffness matrix is obtained.

As the principle of virtual work rate Eq. and the constitutive relationship are linear Eq. of rates, they can be replaced by increments defined with respect to any monotonously increasing measure, such as the tool-displacement increment.

Following the standard procedure of finite elements to form the whole global stiffness matrix,

$$[K]\,\{\Delta u\} = \{\Delta F\} \tag{6}$$

in which

$$[K] = \sum_{\langle e\rangle}\int_{V\langle e\rangle} [B]^T([D_{ep}] - [Q])\,[B]\mathrm{d}V + \sum_{\langle e\rangle}\int_{V\langle e\rangle} [E]^T[G][E]\mathrm{d}V$$

$$\{\Delta F\} = \left(\sum_{\langle e\rangle}\int_{S\langle e\rangle} [N]^T\,\{\dot{\bar{t}}\}\mathrm{d}S\right)\Delta t$$

In these equations, $[K]$ is the global tangent stiffness matrix, $[D_{ep}]$ is the elemental elasto-plastic constitutive matrix, Δu denotes the nodal displacement increment, and $\{\Delta F]$ denotes the prescribed nodal force increment. $[Q]$ and $[G]$ are defined as stress-correction matrices due to the current stress at any stage of deformation.

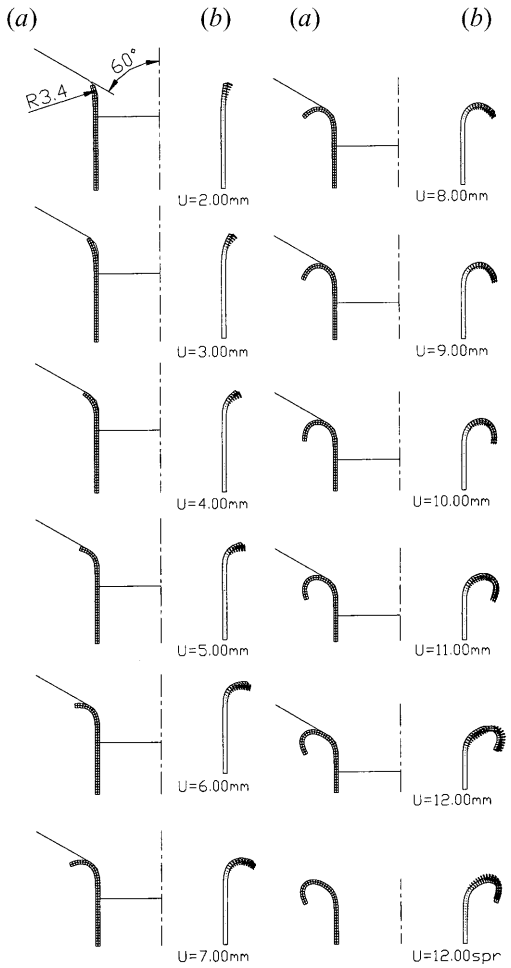

Fig. 2. (*a*) Deformed geometries, and (*b*) nodal velocity distributions in the outward curling of tubes at 12 different forming stages. Hard copper tube, $n = 0.05$; $t_0 = 0.8$ mm; $\alpha = 60°$; $R = 3.4$ mm.

2.2 SRI Scheme

As the implementation of the full integration (FI) scheme for the quadrilateral element leads to an excessively constraining effect when the material is in the nearly incompressible elasto-plastic situation in the forming process [13], Hughes proposed that the strain rate–velocity matrix be decomposed to the dilation matrix $[B]_{dil}$ and the deviation matrix $[B]_{dev}$, i.e.

$$[B] = [B]_{dil} + [B]_{dev} \tag{7}$$

in which the matrices $[B]_{dil}$ and $[B]_{dev}$ are integrated by conventional four-point integration. When the material is deformed to the nearly incompressible elasto-plastic state, the dilation matrix $[B]_{dil}$ must be replaced by the modified dilation matrix $[\bar{B}]_{dil}$ that is integrated by the one point integration, i.e.

$$[\bar{B}] = [\bar{B}]_{dil} + [B]_{dev} \tag{8}$$

in which $[\bar{B}]$ is the modified strain rate–velocity matrix. Substituting Eq. (8) into Eq. (7), the modified strain rate–velocity matrix is

$$[\bar{B}] = [B] + ([\bar{B}]_{dil} - [B]_{dil}) \tag{9}$$

Explicitly, the velocity gradient–velocity matrix $[E]$ is replaced by the modified velocity gradient–velocity matrix $[\bar{E}]$

$$[\bar{E}] = [E] + ([\bar{E}]_{dil} - [E]_{dil}) \tag{10}$$

3. Numerical Analysis

The analytical model of the tube-curling process is axially symmetric. Thus, only the righthand half of the centre axis is considered. Division of the part's finite elements is automatically processed by the computer. Since there is drastic deformation from the bending and curling at the tube's end, a finer element division is required for this section in order to derive precise computation results. The lefthand half shown in Fig. 1 denotes the sizes of the part and die at the beginning. The detailed dimensions are given in Table 1. In the local coordinates, axis 1 denotes the tangential direction of the contact between tube material and the tool, while axis n denotes the normal direction of the same contact. Constant coordinates (X,Y) and local coordinates (l, n) describe the nodal force, displacement and element's stress and strain.

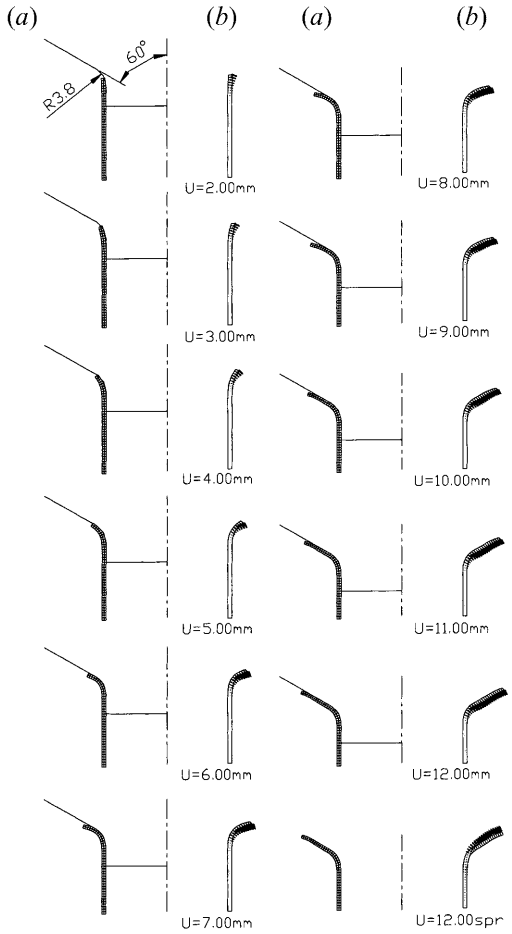

Fig. 3. As Fig. 2, but R = 3.8 mm.

Table 1. Punch angle and radius.

Punch apex angle α (deg.)	Punch radius R (mm)
60	2.0, 2.4, 2.8, 3.1, 3.4, 3.8, 4.1, 4.4, 4.8, 5.1
65	2.4, 2.8, 3.1, 3.4, 3.8, 4.1, 4.4, 4.8, 5.5, 5.4
70	3.1, 3.4, 3.8, 4.1, 4.4, 4.8, 5.1, 5.4, 5.8, 6.1
75	3.4, 3.8, 4.1, 4.4, 4.8, 5.1, 5.4, 5.8, 6.1, 6.4
80	4.8, 5.4, 5.8, 6.1, 6.4, 6.8, 7.2, 7.6, 8.0, 8.4
85	5.8, 6.1, 6.4, 6.8, 7.4, 9.0, 9.4, 9.8, 10.2, 10.6, 11.0

Table 2. Mechanical properties of materials used.

Materials	Outer diameter × thickness	Heat treatment in vacuum	n	F (Mpa)	Yield stress $\sigma_{0.2}$ (Mpa)
Copper	25.4 × 0.8	As received	0.09	380	220
		500°C 1 h	0.53	630	26
		As received	0.05	450	280
		300°C 1 h	0.09	450	260
		400°C 1 h	0.46	610	50
		600°C 1 h	0.50	640	42
70/30 Brass	25.4 ± 0.8	As received	0.18	730	280

$\sigma = F\epsilon^n$; σ = stress; ϵ = strain.

Table 2 gives the material conditions of our simulation. The exterior radius of the tube remains unchanged at 25.4 mm; but there are three different tube wall thickness values, namely, 0.4, 0.6 and 0.8 mm, used in the experiment and computation. The Poisson's ratio and Young's modulus of the hard copper tube are 0.33 and 110740 MPa, respectively. The Poisson's ratio and Young's modulus of brass are 0.34 and 96500 MPa, respectively.

3.1 Boundary Condition

The righthand half of the tube shown in Fig. 1 denotes the deformation shape at a certain stage during the tube-curling deformation. The boundary conditions include the following three sections:

1. The boundary on the FG and BC sections:

$$\Delta f_l \neq 0,\ \Delta f_n \neq 0, \quad \Delta v_n = \Delta \bar{v}_n$$

where Δf_l is the nodal tangential friction forces increment, and Δf_n is the normal force increment. As the material–tool contact area is assumed to involve friction, Δf_l and Δf_n are not equal to zero. Δv_n, which denotes the nodal displacement

increment in the normal direction of the profile of the tools, is determined from the prescribed displacement increment of the punch $\Delta\bar{v}_n$.

2. The boundary on the *CD*, *DE*, *EF*, and *GA* sections:

$$\Delta F_x = 0, \quad \Delta F_y = 0$$

The above condition reflects that the nodes on this boundary are free.

3. The boundary on the *AB* section:

$$\Delta v_x = 0, \quad \Delta v_y = 0$$

The *AB* section is the fixed boundary at the bottom end of the tube. The displacement increment of the node at this location along the *y*-axis direction is set at zero, whereas node *B* is completely fixed without any movement.

As the tube-curling process proceeds, the boundary will be changed. It is thus necessary to examine the normal force Δf_n of the contact nodes along boundary sections *FG* and *BC* in each deformation stage. If Δf_n reaches zero, then the nodes will become free and the boundary condition is shifted from (1) to (2). Meanwhile, the free nodes along the *GA* and *EF* sections of the tube are also checked in the computation. If the node comes into contact with the punch, the free-boundary condition is changed to the constraint condition (1).

3.2 Treatment of the Elasto-Plastic and Contact Problems

The contact condition should remain unchanged within one incremental deformation process, as clearly implied from the interpretation in the former boundary condition. In order to satisfy this requirement, the *r*-minimum method proposed by Yamada et al. [14] is adopted and extended towards treating the elasto-plastic and contact problems [15]. The increment of each loading step is controlled by the smallest value of the following six values.

1. Elasto-plastic state. When the stress of an element is greater than the yielding stress, r_1 is computed by [15] so as to ascertain the stress just as the yielding surface is reached.
2. The maximum strain increment. The r_2 term is obtained by the ratio of the defaulted maximum strain increment ψ to the principal strain increment $d\epsilon$, i.e. $r_2 = \psi/d\epsilon$, to limit the incremental step to such a size that the first-order theory is valid within the step.
3. The maximum rotation increment. The r_3 term is calculated by the defaulted maximum rotation increment β to the rotation increment $d\omega$, i.e. $r_3 = \beta/d\omega$, to limit the incremental step to such a size that the first-order theory is valid within the step.
4. Penetration condition. When forming proceeds, the free nodes of the tube may penetrate the tools. The ratio r_4 [16] is calculated such that the free nodes just come into contact with tools.
5. Separation condition. When forming proceeds, the contact nodes may be separated from the contact surface. The r_5 term [16] is calculated for each contact node, such that the normal component of nodal force becomes zero.
6. Sliding-sticking friction condition. The modified Coulomb's friction law provides two alternative contact states, i.e. sliding or sticking states. Such states are checked for each contacting node by the following conditions:

$$v_l^{rel(i)} \bullet v_l^{rel(I-l)} \geqq 0$$

(a) if $|v_l^{rel(i)}| >$ VCRI, then $f_1 = \mu f_n$, the node is in sliding state

(b) if $|v_l^{rel(i)}| <$ VCRI, then $f_1 = \mu f_n (v_l^{rel}/\text{VCRI})$, the node is in quasi-sticking state.

$$v_l^{rel(i)} \bullet v_l^{rel(I-1)} < 0.$$

The direction of a sliding node is opposite to the direction of the previous incremental step, making the contact node a sticking node at the next incremental step. The ratio r_6 is then obtained here, $r_6 = Tolf/|v_l^{rel(i)}|$, which produces the change of friction state from sliding to sticking, where *Tolf* (= 0.0001) is a small tolerance.

The constants of the maximum strain increment ψ and maximum rotation increment β used here are 0.002° and 0.5°, respectively. These constants are proved to be valid in the first-order theory. Furthermore, a small tolerance in the check procedure of the penetration and separation condition is permitted.

3.3 Unloading Process

The phenomenon of spring-back after unloading is significant in the tube-forming process. The unloading procedure is executed by assuming that the nodes on the bottom end of the tube are fixed. All of the elements are reset to be elastic. The force of the nodes which come into contact with the tools is reversed in becoming the prescribed force boundary condition on the tube, i.e. $\dot{F} = -F$.

Meanwhile, the verification of the penetration, friction, and separation condition is excluded in the simulation program.

4. Results and Discussion

Figure 2 shows the simulation results of curling forming of copper tubes with the punch semi-angle, $\alpha = 60°$, and the arc radius, $R = 3.4$ mm. Figure 2(*a*) denotes the geometric shape of the deformation, in which the last shape is the final shape of the part after unloading. Figure 2(*b*) shows the nodal velocity distribution during deformation. The last diagram shows the nodal velocity distribution after unloading. These figures show that the tube end material enters smoothly along the punch surface at the initial stage. After that, the tube end material gradually bends outward and curls up, resulting in the so-called outward curling forming. Figure 3 shows the simulation result in the case of $R = 3.8$ mm. The tube end material still shows the so-called flaring forming after passing the arc induction section and conical face forming.

Figure 4 shows the result of curling simulation of copper tubes in the case of $\alpha = 75°$ and $R = 6.1$ mm. In contrast, Fig. 5 shows the simulation result of flaring forming in the case of $R = 6.4$ mm.

Figure 6 shows the strain distributions corresponding to those of Figs 2 and 3 at a punch travel of 12 mm. Figure 7

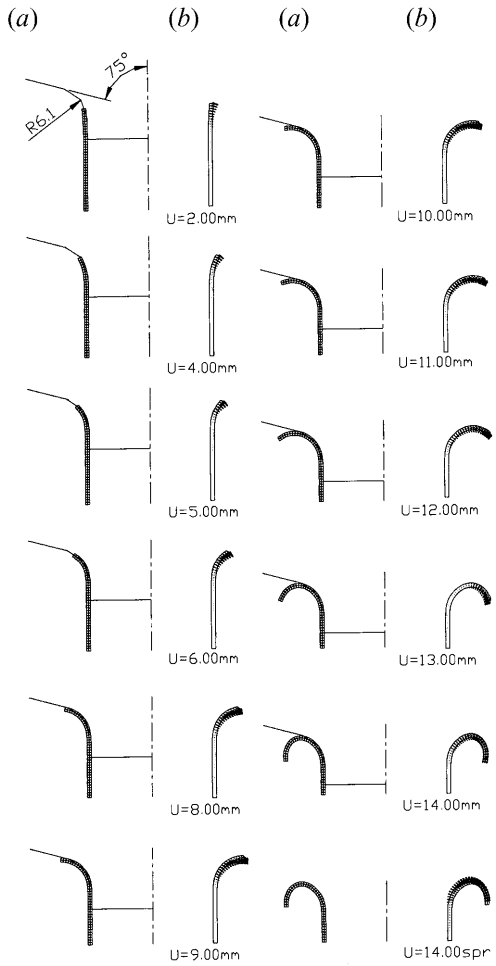

Fig. 4. As Fig. 2, but $\alpha = 75°$; $R = 6.1$ mm.

shows the strain distributions corresponding to those of Figs 4 and 5 at a punch progress of 14 mm. The deformation is mostly the result of pulling in the circumference direction, bending in the meridian direction and shearing in the thickness direction. The maximum diameter of the tube end is the flaring forming. Thus, its strain value in the circumference direction is far greater than that of outward curling. The reduction in tube wall thickness is also more significant in flaring forming. Thus, under the same progress, fracture of the tube end occurs more easily in flaring forming than in other situations.

Figures 8 and 9 show the simulation results for hard copper and brass, respectively. The same tube wall thickness, tube radius, lubrication condition, and half-apex of the punch are used in both simulations. However, different values of the punch arc radius are used, which generate different types of forming, namely, flaring and curling. That is, if the arc radius, ρ, at the punch entrance is greater than the critical bending radius, ρ_C, then the tube end material forms flaring along the punch arc induction section and conical face. On the contrary, if $\rho_C \geqq \rho$, the tube end material leaves the punch surface and forms curling. Both figures show that the critical bending radius increases as the half-apex of the punch increases. A comparison shows that the results of our numerical simulation are identical to the experimental data reported in [12]. The so-called critical bending radius, ρ_C, can be expressed as follows:

$$\rho_C = R_C - \frac{t_0}{2} = \frac{(R_{C\max} + R_{f\min})}{2} - \frac{t_0}{2} \tag{11}$$

where

R_C = punch radius corresponding to ρ_C
$R_{f\min}$ = minimum value of punch radius required to flare
$R_{C\max}$ = maximum value of punch radius required to curl
t_0 = wall thickness of tubes

Figures 10 and 11 show the correlation between the non-dimensional critical bending radius ($\bar{\rho}_C$) and the half apex angle of the punch with two different wall-thickness-to-diameter ratios in the cases of hard copper tube and brass tube, respectively. The value of $\bar{\rho}_C$ can be defined as follows:

$$\bar{\rho}_C = \frac{\rho_C}{\sqrt{(t_0 d_0)}} \tag{12}$$

If $\bar{\rho}_C$ is unrelated to the wall-thickness-to-diameter ratio, then the geometrical similarity law of the critical bending radius

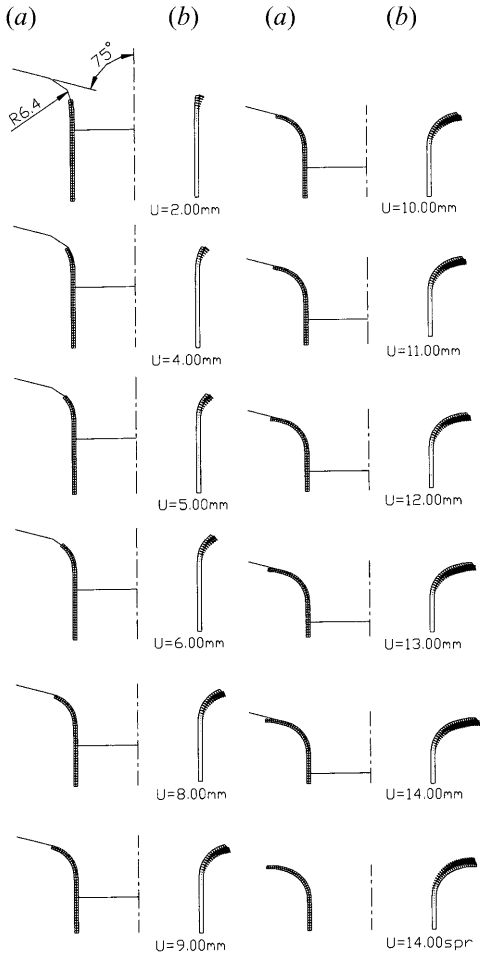

Fig. 5. As Fig. 2, but $\alpha = 75°$; $R = 6.4$ mm.

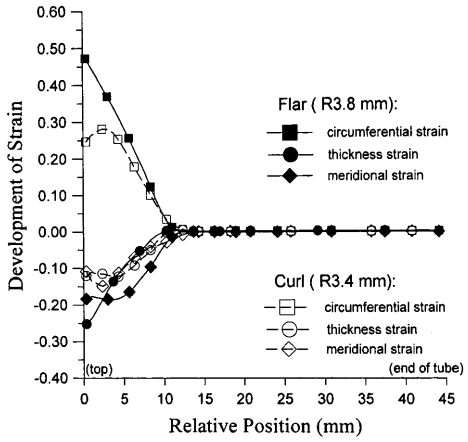

Fig. 6. Comparison of calculated strain distributions under curling and flaring processes. Hard copper tube, $n = 0.05$; $t_0 = 0.8$ mm; $\alpha = 60°$.

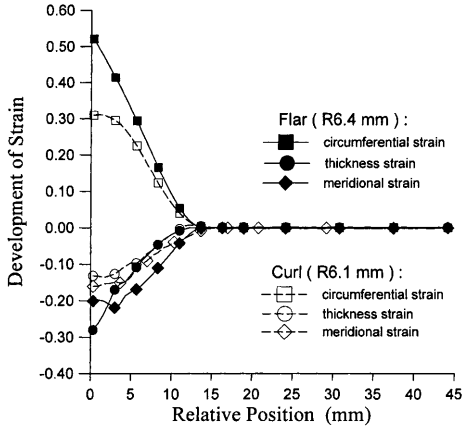

Fig. 7. As Fig. 6, but $\alpha = 75°$.

exists. Judging from the fact that the two curves shown in Figs 10 and 11 are almost identical, we can be certain of the existence of the geometrical similarity law of the critical bending radius of the tube materials.

Figures 12 and 13 show the relationship between the maximum punch radius and half-apex angle of the punch when curling occurs in the numerical simulation of wall thickness values of 0.4, 0.6, and 0.8 mm in the cases of hard copper tube and brass tube, respectively. When values of both the

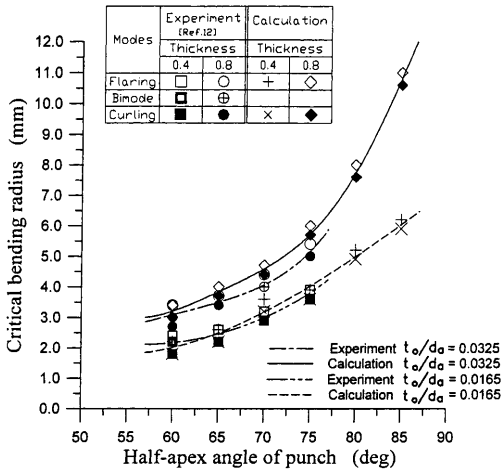

Fig. 8. The effect of tube thickness on the relationship between critical bending radius and punch angle. Hard copper tube, n = 0.05.

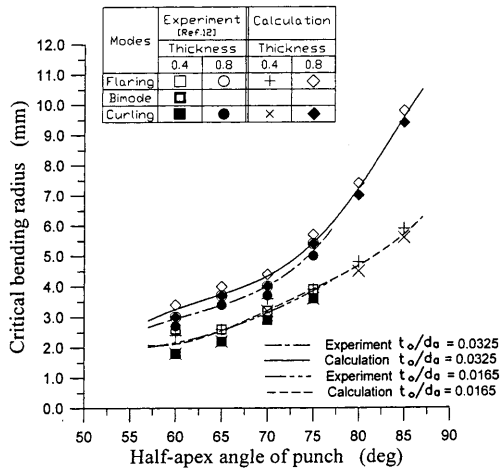

Fig. 9. As Fig. 8, but brass tube, n = 0.05.

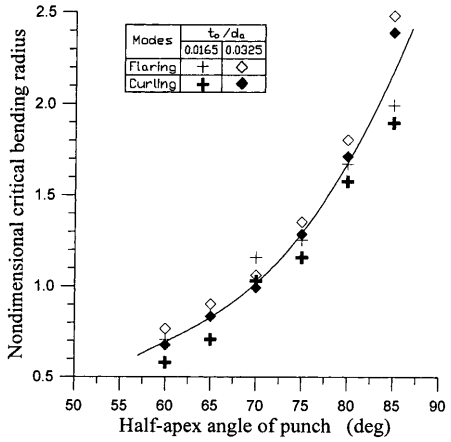

Fig. 10. Non-dimensional critical bending radius – half-apex angle of punch relationships in outward curling of tubes. Hard copper tube, n = 0.05.

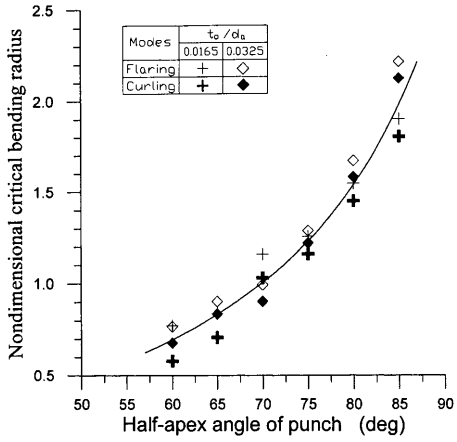

Fig. 11. As Fig. 10, but brass tube, n = 0.18.

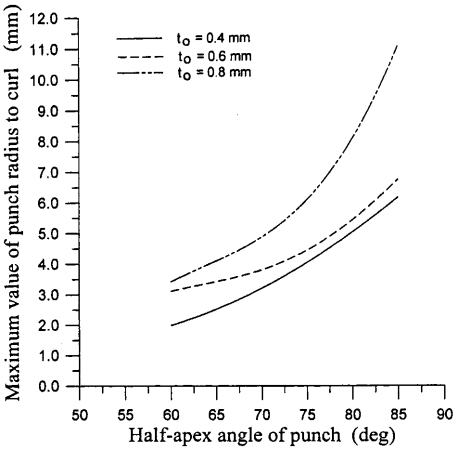

Fig. 12. Maximum radius of punch to curl for various half-apex angles of punch. Hard copper tube, n = 0.05.

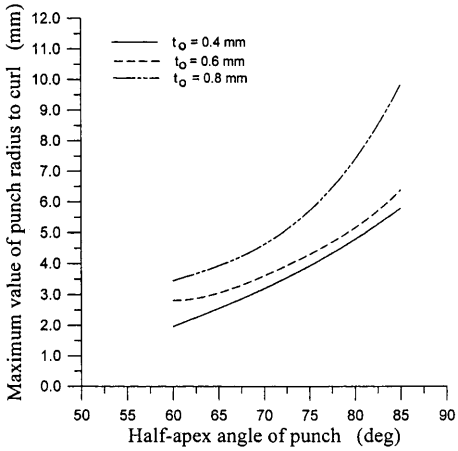

Fig. 13. As Fig. 12, but brass tube, n = 0.18.

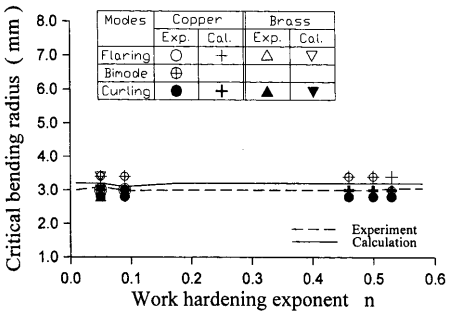

Fig. 14. Dependence of the critical bending radius on the work hardening exponent. $\alpha = 60°$; $t_0 = 0.8$ mm.

radius and the corresponding half-apex angle of the punch fall on the curve, the conditions will lead to flaring. On the other hand, when both values fall below the curve, the conditions will lead to curling. These figures indicate that the maximum punch radius increases as the half-apex angle of the punch enlarges.

Figure 14 shows the correlation between the material's work hardening exponent (n) and the critical bending radius. Regardless of the variation in n value between 0.03 and 0.53 owing to different tube materials, results of the numerical simulation indicate that the value of the critical bending radius remains constant, thus forming a straight line. These findings are almost identical to the experimental data shown in [12], and it implies that the critical bending radius at the time of curling is unrelated to the work hardening exponent.

Figure 15 shows the effects of lubrication on the relationships between the critical bending radius and half-apex angle of the punch. The critical bending radius increases with the increasing half-apex angle of the punch in the case of $\mu = 0.05$ and $\mu = 0.20$. Furthermore, the result revealed that there is a negligible difference in the magnitude of the critical bending radius between the two lubricant conditions.

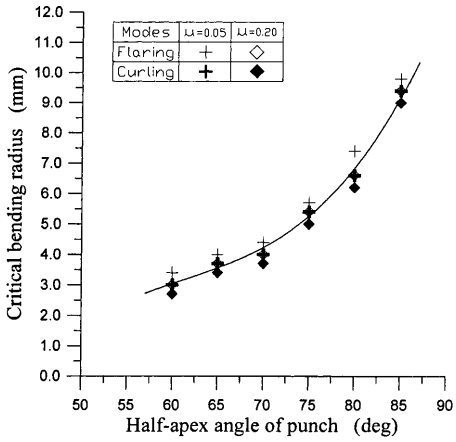

Fig. 15. Dependence of the critical bending radius on lubricating conditions. Brass tube, $t_0 = 0.8$ mm.

5. Conclusion

An elasto-plastic finite-element computer code was developed from the updated Lagrangian formulation to simulate tube-curling with a conical punch process. The high nonlinearity of the process was taken into account in an incremental manner and an $r_{\min}$ technique was adopted to limit the size of each increment step for a linear relation.

The modified Coulomb's friction law developed is a continuous function. As discussed earlier, this function can handle the sliding and viscosity phenomena of the tool and metal interface that are difficult to describe with the ordinary discontinuous friction model. The SRI finite-element is the four-node-quadrilateral element in four integration points. Then the SRI coupled with the finite-element large deformation analysis is further applied successfully to the analysis of the conical tube-curling formation process. According to the above analyses and discussion, the following conclusions can be drawn:

1. A critical bending radius, ρ_C, exists. If the arch radius, ρ, at the punch entrance is larger than the critical bending radius, ρ_C, then the tube end material travels along the punch arch induction part and the conical face to form flaring. On the other hand, if $\rho_C \geqq \rho$, the tube end material leaves from the punch surface and results in curling. The value of the critical bending radius increases as the half-apex angle of the punch increases.
2. The critical bending radius, ρ_C, follows the geometrical similarity law. The value of ρ_C increases as the half-apex angle of the punch increases. We also learned that the value of ρ_C is not correlated with the tube material, lubrication conditions or the wall-thickness-to-diameter radius ratio.
3. The circumference strain of flaring is greater than that of curling. Flaring also has greater reduction in thickness than curling. Thus, tube end fracture occurs more easily in flaring. In contrast, products with curling can guarantee handling safety and reinforce the end portion of tube materials.
4. The die shape is expressed as a numerical function. Thus, the finite-element model developed in this study can be used in the continuous shape of any tools and employed to simulate all types of flaring or curling processes.

References

1. A. Nadai, "Plastic state of stress in curved shells: the forces required for forging of the nose of high-explosive shell, forming of steel shells", Presented at the annual meeting of the ASME, New York, USA, November 23–December 1, 1943.
2. A. K. Cruden and J. F. Thompson, "The end closer of backward extruded cans", NEL Report NO.511, National Engineering Laboratories, Glasgow, Sweden, 1972.
3. K. Manabe and H. Nishimura, "Forming loads and forming limits in conical nosing of tubes – study on nosing and flaring of tubes I", Journal Japan Society for Technology of Plasticity, 23 (255), pp. 335–342, 1982–4.
4. K. Manabe and H. Nishimura, "Experimental study on stress and strain distributions in conical nosing of tubes – study on nosing and flaring of tubes II", Journal Japan Society for Technology of Plasticity, 23 (255), pp. 335–342, 1982–4.

5. K. Manabe and H. Nishimura, "Analysis of stresses and forming loads in conical nosing of tubes – study on nosing and flaring of tubes III", Journal Japan Society for Technology of Plasticity, 23 (258), pp. 650–657, 1982–7.
6. K. Manabe and H. Nishimura, "Forming loads in tube-flaring with conical punch – study on nosing and flaring of tubes V", Journal Japan Society for Technology of Plasticity, 24 (264), pp. 47–52, 1983–1.
7. K. Manabe and H. Nishimura, "Stress and strain distributions in tube-flaring with conical punch – study on nosing and flaring of tubes VI", Journal Japan Society for Technology of Plasticity, 24 (264), pp. 276–282, 1983–3.
8. M. C. Tang and S. Kobayashi, "An investigation of the shell nosing process by the finite element method, Part 1: Nosing at room temperature (cold nosing)", Transactions ASME, Journal of Engineering for Industry, 104, pp. 305–311, 1982.
9. Y. M. Huang, Y. H. Lu and M. C. Chen, "Analyzing the cold nosing process using elasto-plastic and rigid-plastic methods", Journal of Materials Processing Technology, 30, pp. 351–380, 1992.
10. K. Kitazawa and M. Kobayashi, "Experimental study of deformation mechanism in tube-end curling – curling of shells II", Journal Japan Society for Technology of Plasticity, 28 (323), pp. 1267–1274, 1987–12.
11. K. Kitazawa, M. Kobayashi and S. Yamashita, "Elementary energy analysis of tube-end curling – theoretical analysis of tube and conical shell end curling I", 29 (331), pp. 845–850, 1988–8.
12. K. Kitazawa, "Criteria for outward curling of tubes", Transactions ASME, Journal of Engineering for Industry, 115, pp. 466–471, 1993.
13. J. C. Nagtegaal, D. M. Parks and J. R. Rice, "On numerically accurate finite element solutions in the fully plastic range", Transactions on Computational Methods in Applied Mechanical Engineering, 4, pp. 153–177, 1974.
14. Y. Yamada, N. Yoshimura and T. Sakurai, "Plastic stress strain matrix and its application for the solution of elasto-plastic problems by the finite element method", International Journal of Mechanical Sciences, 10, pp. 343–354, 1968.
15. A. Makinouchi, "Finite element modeling of draw-bending process of sheet metal", in K. Mattiasson, A. Samuelsson, R. D. Wood and O. C. Zienkiewicz (eds), Proceedings NUMIFORM'86 Conference, Gothenburg, pp. 327–332, 1986.
16. Y. M. Huang, Y. H. Lu and A. Makinouchi, "Elasto-plastic finite element analysis of V-shape sheet bending", Journal of Materials Processing Technology, 35, pp. 129–150, 1992.